Focusing with Two-Dimensional Angular-Symmetric Circular Acoustic Lenses[1]

Olgun Adem Kaya[a], Ahmet Cicek[b, c], and Bulent Ulug[c]

[a] *Department of Computer Education Technologies, Faculty of Education, Inönü University,*
Campus 44280, Malatya, Turkey

[b] *Department of Physics, Faculty of Arts and Sciences, Mehmet Akif Ersoy University,*
15100 Burdur, Turkey

[c] *Department of Physics, Faculty of Science, Akdeniz University,*
Campus 07058, Antalya, Turkey

e-mail: oakaya@inonu.edu.tr

Received June 8, 2010

Abstract—Focusing properties of an acoustic lens based on a modified triangular sonic crystal slab whose columns are aligned on concentric arcs of equal radial distance are investigated. Capability of focusing normally-incident plane waves is demonstrated by means of Finite Element Method. Focusing mechanisms are discussed on the basis of band structures and equifrequency contours considering a model where triangular lattice is elongated along ΓK direction. Focusing behavior of the proposed lens is argued to arise from negative refractions at the air-lens interfaces accompanied by index guiding in its interiors. Wavelength-order confinement in the transverse direction is observed. Double focusing is attributed to geometrical effects and contribution of self guiding is discussed. Possibility of occurrence of birefraction at the input face of the lens together with positive refraction at the output face is also discussed.

1. INTRODUCTION

In analogy with photonic crystals (PC), sonic crystals (SC) are artificial structures composed of periodic arrangement of acoustic scatterers. Depending on crystal parameters and wave frequency, interaction of acoustic waves with a SC results in formation of forbidden zones in the band structure (BS) [1–5]. Similar to a "double-negative" medium [6], negative refraction can take place at the interface of a homogeneous medium and a SC [7–11]. Negative refraction can be deduced from equifrequency contours (EFC), as the direction of the group velocity is determined by the gradient of angular frequency with respect to wave vector [9–11]. Beside negative refraction in SCs, imaging and focusing properties of flat SC lenses are experimentally demonstrated on triangular lattices of steel cylinders in air [8] and water [9], respectively.

Curved surfaces of either continuous media [12] or SCs that mimic the geometry of homogeneous optical lenses are capable of focusing acoustic waves through positive refraction at the interfaces with host media [13, 14]. On the contrary, negative refraction properties of SCs have been utilized in designing flat SC lenses (SCL) though Håkansson et al demonstrated in

an aperiodic distribution of scatterers that negative refraction is not a requisite for sound focusing [15]. Flat PC [16–19] and SC lenses relying on negative refraction can image point sources in their vicinities. Far field imaging [20, 21] of a point source by a flat SC with sub-wavelength resolution at very small source distances [22] are demonstrated. However, such lenses suffer from restricted range of operation, large focal zones, and inability to focus a normally-incident plane wave. Focusing issue is treated by employing either curved surfaces [13, 14, 23, 24] or a gradient in the effective index of refraction that could be achieved in different ways such as gradually modifying the lattice constant [25, 26], the filling fraction [27–30] or the density of material [27, 30], all relying on band structure engineering. Playing with the band structure might lead to overlapping of subsequent bands, where possibility of refraction of an incident wave to different angles emerges. Double focusing in certain cases is attributed to this phenomenon which is called negative birefraction [11].

Feng et al. [7, 10] investigated dependence of refraction angle on frequency and the angle of incidence in SCs and demonstrated that the negative angle of refraction increases as the angle of incidence and frequency increase. In case of a point source very close

---

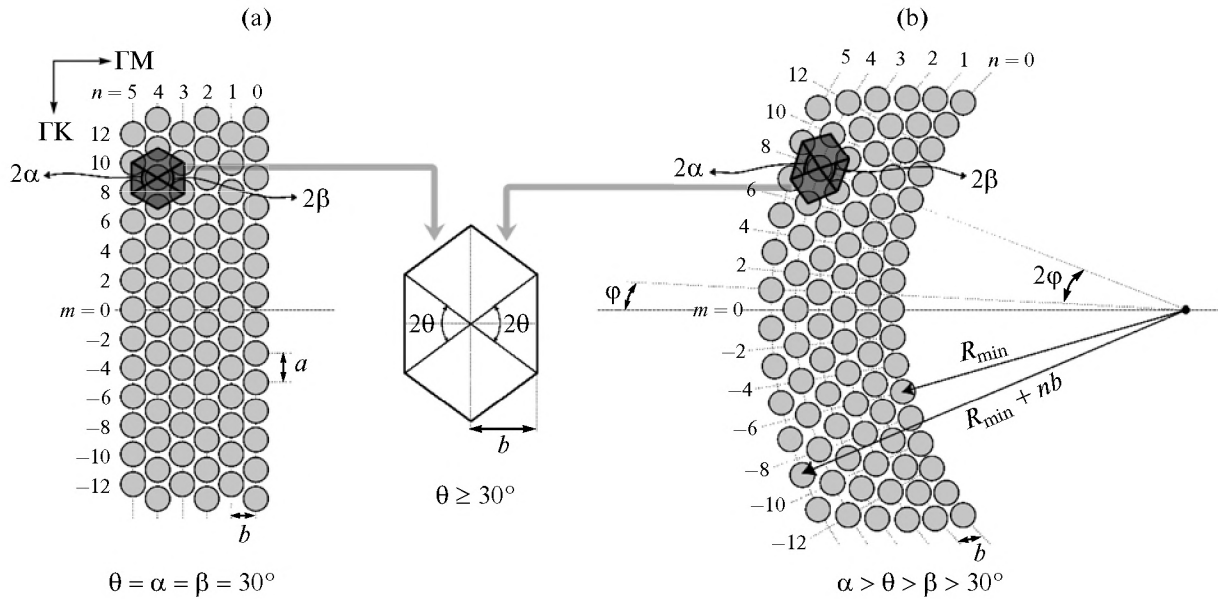[1] The article is published in the original.

Fig. 1. Structure and design parameters of (a) triangular lattice and (b) ASCAL, where close-up of the hexagonal unit considered in BS and EFC calculations is demonstrated in between.

to a SC slab, angle of incidence of the acoustic wave ranges from 0° to 90°, while the incident wave vector may span a quadrant of the first Brillouin zone (BZ). As the point source moves away from the SC, however, angle of incidence sweeps a narrower range and reaches its limiting value, i.e., 0°, at a sufficiently long distance. Since the angle of incidence in this case is well defined, only a single wave vector normal to the interface couples to the SC, yielding no focusing. One way of achieving focusing of normally incident acoustic plane waves is bending a flat SC so that angle of incidence, which is defined by the curvature and the width of the structure, can take nonzero values. In this case, even though the incident wave is described by a single well-defined wave vector, it can be refracted at different angles corresponding to different wave vectors on different "units."

Based on the arguments presented above, focusing properties of an acoustic lens called angular symmetric circular acoustic lens (ASCAL) after its design, which is obtained by modifying a triangular SC slab in such a way that columns of the slab are mapped into concentric circular arcs of equal distance are investigated. Analyses are carried out by computing the steady-state solutions for sound pressure level through Finite Element Method (FEM). It is demonstrated that a normally-incident plane wave can be focused with a resolution of the order of wavelength. Mechanisms responsible for acoustic focusing in ASCAL are discussed using a model in which triangular units on different layers are elongated likewise in the direction normal to the interface through inspection of corresponding BSs and EFCs.

2. GEOMETRY AND COMPUTATIONAL METHODS

Proposed lens aims to achieve acoustic focusing through mapping a triangular SC slab consisting of steel cylinders in air into a circular arc to vary the angle of incidence quasi-continuously for a single well-defined wave vector in air. The SC slab, whose lattice constant is $a = 25$ mm, consists of 6 columns of scatterers with 10.5 mm radii (corresponding to a filling fraction of 64%) normal to the ΓM direction and it is demonstrated in Fig. 1a. Adopted material parameters are $\rho_{steel} = 7800$ kg/m³, $\rho_{air} = 1.21$ kg/m³ for densities and $c_{steel} = 6100$ m/s, $c_{air} = 334.5$ m/s [7] for longitudinal speeds of sound in the homogeneous media, respectively. With these design parameters, the triangular SC slab is observed to be capable of imaging a point source in its vicinity in a frequency range of $8-12$ kHz via negative refraction in the second band of its BS.

Transformation of SC slab to ASCAL is carried out by mapping each layer (column) n into a circular arc of radius $R_{min} + nb$, as depicted in Fig. 1b. The innermost layer, $n = 0$, lies on a radius of curvature R_{min} while the radial increment between two successive layers is $b = a\sqrt{3}/2$. The angle between the radial lines connecting the centers of two adjacent cylinders located along successive even and odd numbered rows to the center of curvature is denoted by φ. It should be noted that, contrary to its flat counterpart, none of the units (denoted by hexagons) in Fig. 1b is regular and identical to another for any m, where m indicates the position of rows with respect to acoustic axis. The angle at which the radial direction connecting the central cyl-
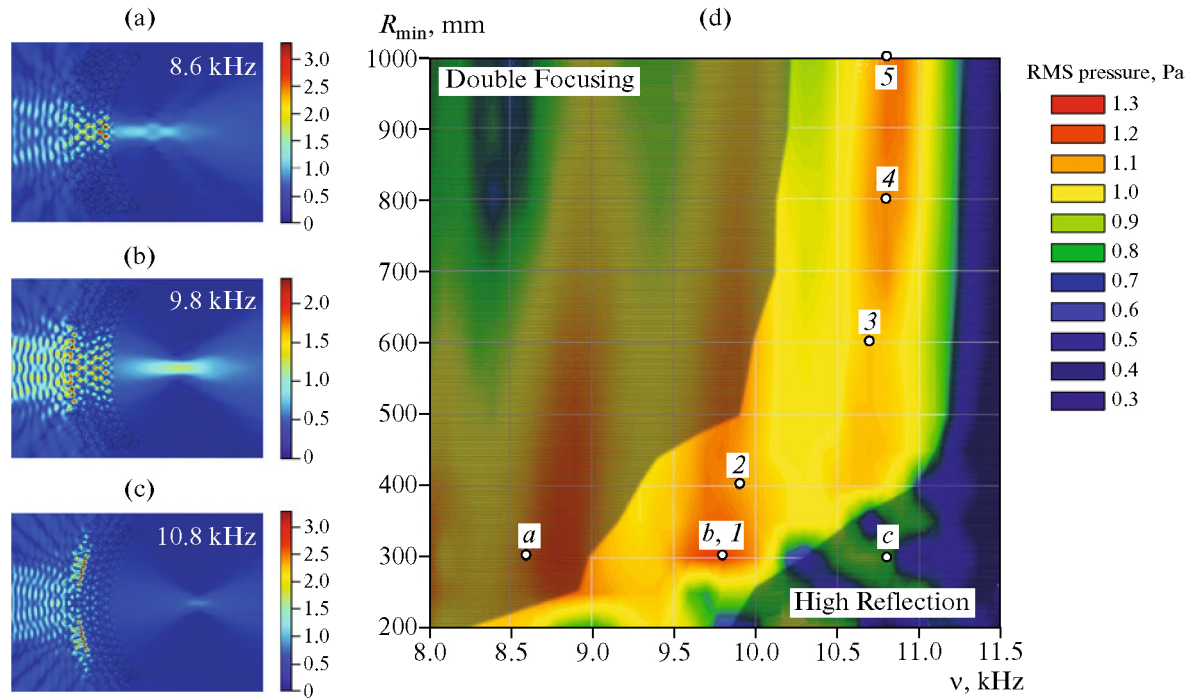
Fig. 2. Distribution of RMS acoustic pressure for $R_{min} = 300$ mm at (a) 8.6 kHz, (b) 9.8 kHz, and (c) 10.8 kHz along with (d) 2D filled contour plot of P_{RMS} at the primary focal zone of ASCAL with respect to R_{min} and ν, where $a-c$ and $1-5$ indicate the points corresponding to the cases in (a) to (c) and in Fig. 4, respectively.

inder of a selected unit to the centre of curvature makes with the acoustic axis is $m\varphi$ and defines the angle of incidence for a plane wave incident along the acoustic axis for that particular unit.

Although none of the "units" with four unequal edges out of six in Fig. 1b are regular hexagons, they can be approximated for simplicity by hexagons which are elongated normal to ΓM direction. Elongation can be defined by $E(\theta) = [\tan(\theta)/\tan(30°)] - 1 = \sqrt{3}\tan(\theta) - 1$, where θ is the average of angles between the lines connecting the centers of cylinders at sites (m, n) and $(m \pm 1, n \pm 1)$, i.e., α and β, as shown in the close-up in Fig. 1. Note that, elongation fades away and "units" on ASCAL are reduced to regular hexagons for $\theta = 30°$ in the limit $R_{min} \longrightarrow \infty$. Following the definitions presented above, it is seen from Fig. 1 that ASCAL provides not only a quasi-continuous angle of incidence for a plane wave but also a gradient of filling fraction with n which increases as n approaches 0.

Focusing properties of ASCAL are investigated as a function of R_{min} in the range from 300 mm to 1000 mm. Steady-state solutions of the acoustic wave equation in two dimensions (2D) are obtained through FEM computations and confirmed by Finite-Difference Time-Domain (FDTD) simulations. The computational domain is excited by a plane wave source whose width (w) is 200 mm and amplitude is 1.0 Pa.

3. PLANE WAVE FOCUSING

The proposed lens is observed to focus the plane wave incident along the acoustic axis. Figures 2a to 2c demonstrate that two distinct foci appear at low frequencies, overlap in a moderate frequency range and diminish considerably due to strong reflections at high frequencies for a particular R_{min}. Thus, P_{RMS} at the primary focal zone of ASCAL is recorded with respect to R_{min} by varying the frequency between 8 kHz and 12 kHz in steps of 0.1 kHz. Results are demonstrated in Fig. 2d, where efficient acoustic focusing is accomplished outside the shaded regions. The region denoted by "Double focusing" on the top-left part of Fig. 2d refers to the range where two distinct focal points are easily distinguishable as in Fig. 2a. The origins of double focusing are discussed later. The "High reflection" region on the bottom-right corner in Fig. 2d refers to a range of R_{min} and ν where acoustic pressure at the focal points drops drastically below a specific value, as seen in Fig. 2c.

The un-shaded region appropriate for "single" focusing moves to higher frequencies as R_{min} increases up to 500 mm beyond which, ASCAL approaches conventional slab lens and increase in R_{min} does not make a significant difference.

Sound pressure diagrams for the steady state solutions obtained for ASCAL, as well as transverse and longitudinal pressure distributions at the focal zones for optimal frequencies corresponding to different
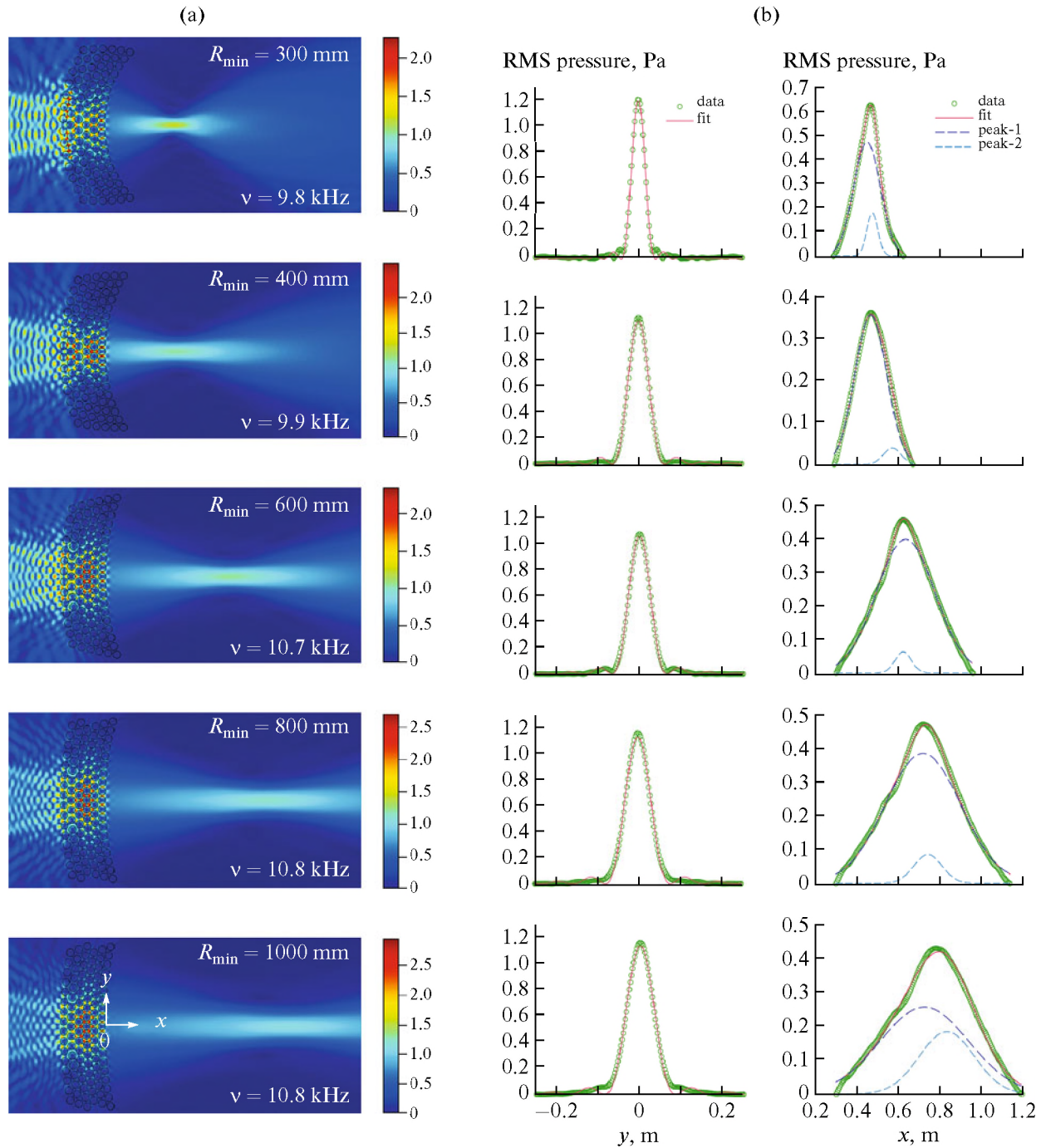
Fig. 3. From top to bottom: (a) sound pressure diagrams for R_{min} and ν values marked by *1–5* in Fig. 2d, (b) pressure distributions fitted by (left) $|sinc(cx)|$ in the transverse direction and (right) two Gaussians along the acoustic axis. *y* and *x* represent the distances from the peak position of the primary focus and the inner vertex of ASCAL, respectively.

R_{min}, which are marked on Fig. 2d as *1–5*, are depicted in Fig. 3. Focusing quality is assessed by fitting $|sinc(cx)|$ function where c is a constant, to the transverse pressure distribution of the primary peak at the focal zone as seen in Fig. 3b. Although sub-wavelength resolution is not achieved, data in Fig. 3b clearly demonstrate that ASCAL effectively focuses plane waves to

spot sizes on the order of λ_{air}: 1.11, 1.65, 1.91, 2.26 and 2.45λ_{air} for R_{min} = 300, 400, 600, 800, and 1000 mm, respectively.

It is seen in Fig. 3 that focal distance, as well as longitudinal and transverse extents of the focal zone, increases with increasing R_{min}. This is expected since ASCAL approaches a flat SC for high R_{min} values,
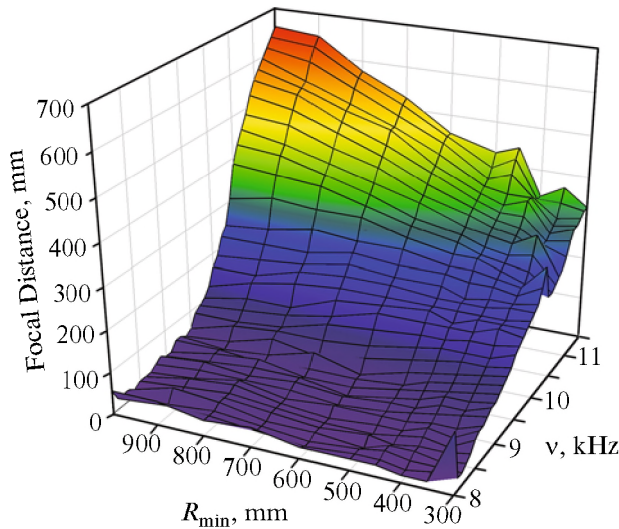
Fig. 4. Variation of primary focal distance with R_{min} and frequency of the incident plane wave.

where its capability of focusing plane waves diminishes. Another observation in Fig. 3a is that focal zone is constituted by the superposition of two elongated peaks whose amplitudes and widths vary with R_{min} and v. This is clarified in the right panel of Fig. 3b, where sound pressure distributions on the focal zones along the acoustic axis are fitted by two Gaussian peaks. It is evident that double foci appear even in the un-shaded region of Fig. 2d, indicating that more than one mechanism might be responsible for the focusing of ASCAL. Since the amplitude of the peak closer to ASCAL is larger, it is called "primary." Both peaks become broader and shift away from the lens as R_{min} increases. In addition, distribution of sound pressure inside ASCAL in Fig. 3a suggests that negative refraction might be taking place in the air-lens interfaces, which will be discussed later. Variation of the primary focal distance measured from the inner vertex of ASCAL with R_{min} and v depicted in Fig. 4 reveals that focal distance increases with increasing R_{min} and v. Although the observed R_{min} dependence of the focal distance is expected as explained above, it obeys no formulable relations, such as the lensmaker's formula [14].

Focusing mechanisms of ASCAL are investigated through the BSs and EFCs of flat SCs which are constructed by approximating the "units" in Fig. 1b with hexagonal cells corresponding to different elongations; $E(30°) = 0$, $E(34°) = 0.17$, and $E(38°) = 0.35$ for $R_{min} = 300$ mm. BSs and EFCs of three lowest-lying bands of elongated SCs computed by the FEM-based method are also calculated through the rigorous Multiple Scattering Theory (MST) for comparison, and no significant differences between the results of these two methods are observed. BSs and EFCs of elongated SCs are presented in Fig. 5a and Fig. 5b,

respectively. Note that for $E(θ) > 0$ ($θ > 30°$, see the close up in Fig. 1), corresponding 1st Brillouin Zone (1BZ) is no longer a regular hexagon but is squeezed in the direction of elongation. Thus, the high-symmetry points are no longer just $Γ$, K, and M but $Γ$ with two inequivalent K (K_1, K_2) and M (M_1, M_2) points as indicated in Fig. 5b. EFCs of the second and the third bands are provided on the left and right panels of Fig. 5b, respectively. The dispersion line in air is displayed as solid lines along the $Γ$–M_1 direction in Fig. 5a, while the EFCs in air for $v = 10.0$ kHz (dashed circles) are presented in Fig. 5b.

Figure 5a reveals that the bands shift to lower frequencies as elongation increases. Besides, the third band approaches the second band, where they begin to share a frequency range for $E(34°) = 0.17$. Moreover, the shape of the second band along $Γ$–K_i and $Γ$–M_i ($i = 1, 2$) directions and the intersection of the dispersion line in air with this band suggest that the second band is accessible for negative refraction for frequencies in the range roughly from 8 kHz to 12 kHz.

Figure 5b demonstrates that the 1BZ is compressed along the $Γ$–K_2 direction normal to $Γ$–M_1, for $E(θ) > 0$. Hence, the circular EFCs observed at high frequencies in the second band for $E(30°) = 0$ no longer exist and some degree of anisotropy is introduced as elongation increases. This leads to reduction of the critical angle determined by the angle of incidence for which the conservation line is tangential to the corresponding EFC for a particular frequency. Moreover, reduction in the curvature of EFCs along the $Γ$–K_2 direction as the elongation increases results in higher negative angles of refraction determined by the angle between the group velocity vectors (v_g) and the surface normal ($Γ$–M_1 direction). Furthermore, in addition to shifting of second and third bands in Fig. 5a to lower frequencies with increasing elongation, the gap between them closes and the top of the second band around the $Γ$ point as well as the point where the two bands anticross is flattened. As a consequence of this, flat portions in the EFCs around $Γ$ point appear and prevail especially for the highest frequencies of the second band and the lowest frequencies of the third band as elongation increases, suggesting the possibility of self collimation [30, 31].

To put the above discussions in a quantitative base, angle of refraction ($φ_{ref}$) for an angle of incidence ($φ_{in}$) of 6° at $v = 10.0$ kHz are calculated for three elongations representative of the cases on the outer, middle and inner layers of ASCAL. Selected value of $φ_{in}$ is close to the critical angle for the second band at that frequency for $E(38°) = 0.35$. Calculated $φ_{ref}$'s are $-20°$, $-35°$, and $-81°$ for elongations 0, 0.17, and 0.35, respectively. On the other hand, the incident wave is refracted positively at $φ_{ref} = 66°$ if the third band for $E(38°) = 0.35$ is considered. Thus, for this elongation, incident wave making small angles with the surface, i.e., for $m < 3$ in Fig. 1b, can be birefracted [11]
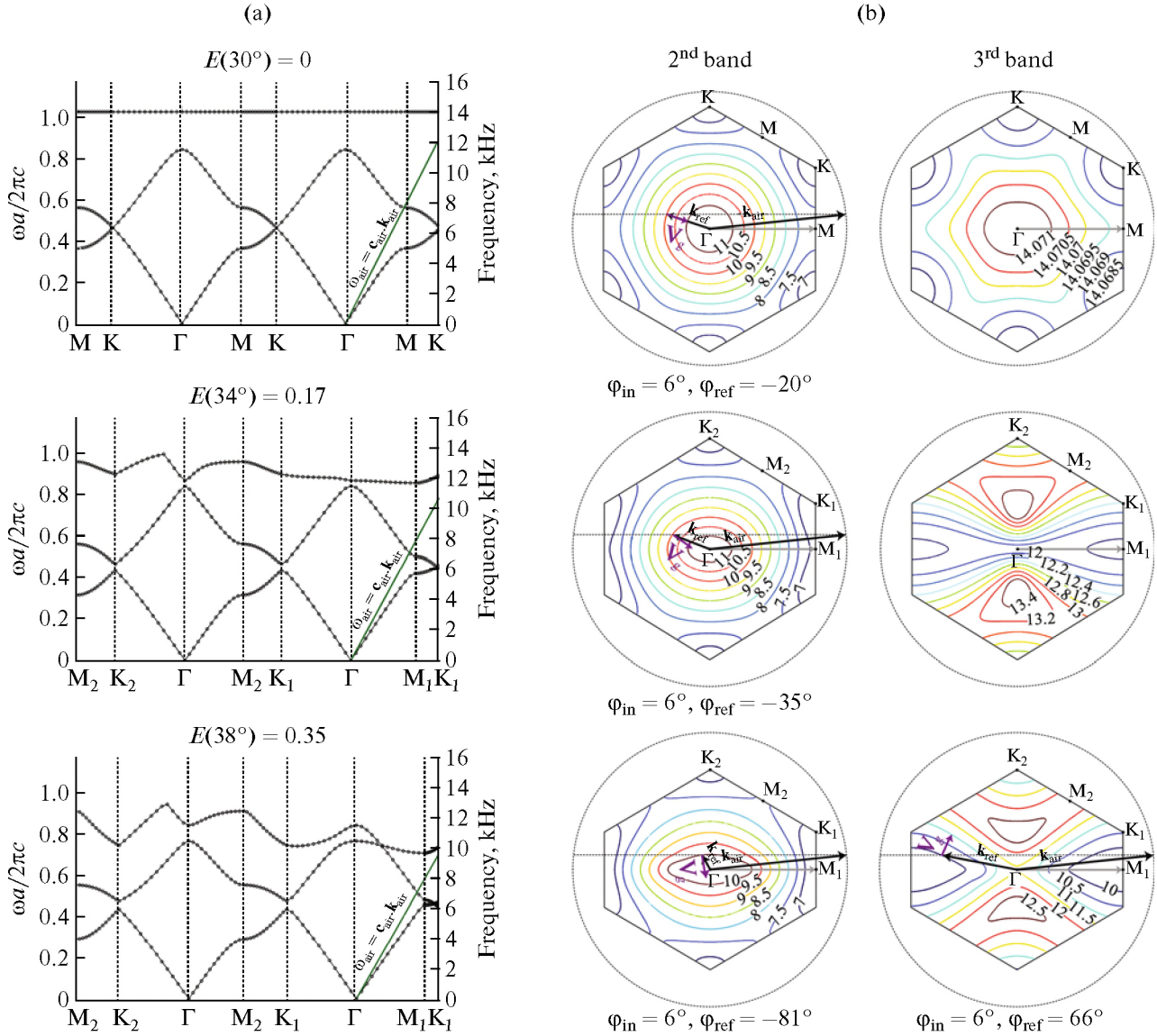
Fig. 5. (a) BSs of triangular SC for different elongations. (b) Corresponding EFCs of the (left) second and (right) third bands on which the inequivalent symmetry points are indicated and the EFCs in air for $\nu = 10.0$ kHz are denoted by dashed circles. Incident and refracted **k** vectors as well as the group velocities are denoted by arrows, while the conservation line is marked as the horizontal dashed line. The grey horizontal arrows indicate the $\Gamma-M_1$ direction.

by the SC leading to appearance of two beams at the output interface. The corresponding effective indices (n_{eff}) are -0.33 ($E = 0$), -0.29 ($E = 0.17$), and -0.12 ($E = 0.35$) for negatively refracted waves at the second band, and 0.55 ($E = 0.35$) for positively-refracted wave at the third band. It is seen from these calculations and geometry of ASCAL that the maximum angle of incidence accepted by the lens is around $6°$ for $R_{min} = 300$ mm at 10 kHz. It is evident in EFCs in Fig. 5b that parts of the incident wave close to the acoustic axis are transmitted while the outer parts are reflected at high frequencies. Therefore, the choice of source width depends on the frequency range of operation and R_{min}, which defines the degree of elongation.

Since the angle of refraction and the effective index at a particular frequency vary with elongation, a tandem design of gradually decreasing elongation—thus increasing filling fraction—might lead to imaging of a point source with higher numerical aperture. Although discontinuities in periodicity along the interfaces are a major issue in such a design, their influence can be subsided by keeping the gradient small. In comparison, due to its curved surface ASCAL provides continuous variation for the angle of incidence for plane waves, i.e., from $0°$ to an angle primarily defined by its height and curvature, along with matching of interfaces corresponding to different elongations.
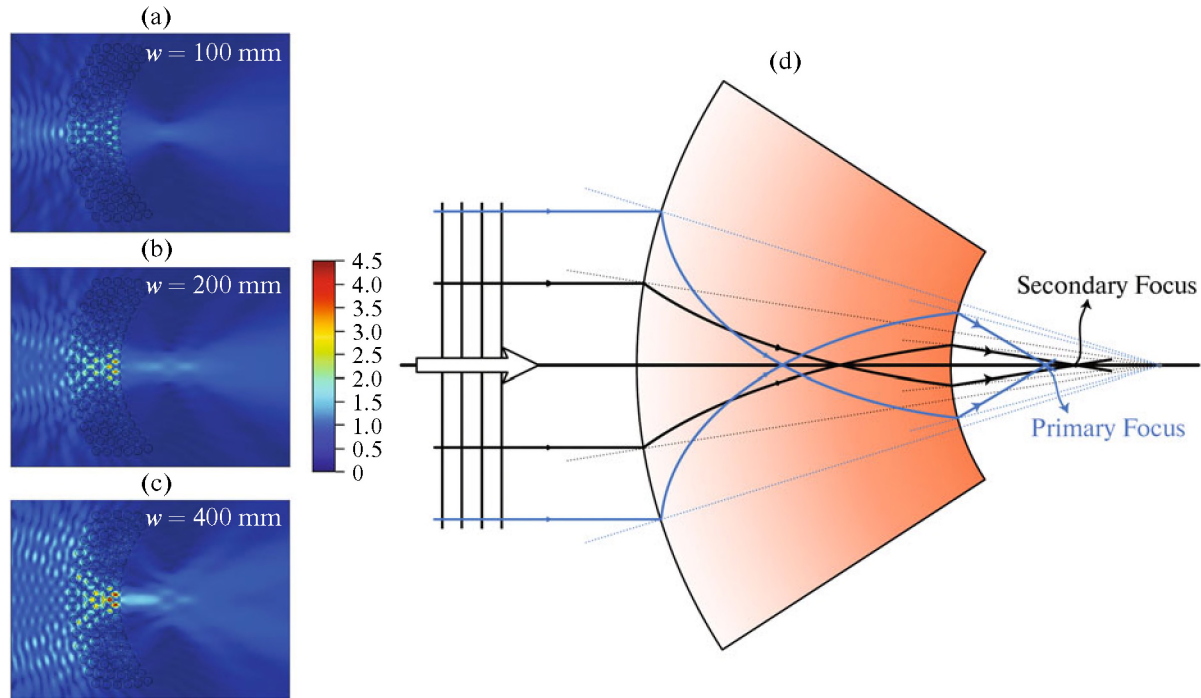
Fig. 6. RMS pressure distribution for w (a) 100 mm, (b) 200 mm, and (c) 400 mm with (d) a pictorial demonstration of focusing mechanism of ASCAL.

Double focusing mechanism of ASCAL are investigated for $R_{min} = 300$ mm and $\nu = 8.7$ kHz (in Double focusing region of Fig. 2d) by varying w. Figures 6a-to-6c demonstrate the result for $w = 100$ mm ($4a$), $w = 200$ mm ($8a$) and $w = 400$ mm ($16a$), respectively. It is seen that, a single focal zone close to the lens appears for $w = 100$ mm, while two distinct foci appear for wider sources. Furthermore, intensity of the primary focus increases as w increases, while that of the secondary focus does not alter much. Thus, it can be concluded that wave portions emanating from the source close to acoustic axis are focused further than those at the edges. The reason for this can be seen in EFCs of the second band for $E = 0.35$, as the absolute value of φ_{ref} increases rapidly to 90° if the angle of incidence is increased to critical value.

Above interpretation also explains the elongation of the focal zone along the acoustic axis, especially for large R_{min}. The occurrence of distinct foci can be understood if one imagines a lens made up of a material with gradually-varying effective index of refraction, as in Fig. 6d. In such a case, rays would leave the lens in a manner to yield a continuous distribution over the focal zone, thus yielding a single focus. However, ASCAL is composed of concrete scatterers with high densities, into which acoustic waves cannot penetrate. Therefore, waves leaving lens can emerge from a few discrete sites, which subtend small angles around the center of curvature, to contribute to the formation of focal zone. This leads to formation of distinct foci, as depicted in Fig. 6d.

Flat portions of EFCs are demonstrated to play a crucial role in acoustic canalization in 2D SCs [32]. Examination of Fig. 6b for no elongation ($\theta = 30°$) in case of the second band reveal that EFCs centered around the Γ point lose their circular shape, approaching hexagons, as they move away from the Γ point, i.e., as their frequencies decrease. Besides, the flat portions are reduced as approaching to the K point. As the elongation increases, EFC for each frequency moves inwards and flat portions arise at high frequencies around the Γ point whereas the ones around K_i points are enlarged. Similar flat regions also appear for the third band with increasing elongation. On the other hand, curvature of EFCs around the Γ point increases at the proximity of the $\Gamma-M_1$ direction. Therefore, self collimation might be another factor contributing to the formation of dual foci. For instance, if φ_{in} is between approximately 2° and 6° for $E = 0.35$ incident waves are self collimated, whereas incidences below 2° result in a spread in the angle of negative refraction. In other words, central portions of the incident wave contributing to the secondary focus in Fig. 6d suffer larger spread upon refraction by the outermost "units" of ASCAL, while the outer portions of the incident wave constituting the primary focus are self collimated and this, in turn, leads to larger intensity of the primary focus.

Overlapping of two foci at high frequencies, as in Fig. 2d, can be understood if the negative-dispersive behavior depicted in Fig. 4 and the EFCs in Fig. 5b are taken into account. While, both foci move away from

the lens with increasing frequency, waves with **k** vectors almost parallel to $\Gamma-M_1$ direction incur less deviation than those with larger angles since the direction of $\mathbf{v}_g$ around the conservation line is modified more extensively with frequency for larger angles of incidence.

Note that for the observed focusing behavior to occur, rays must arrive to ASCAL-air interface at the output below the surface normal, as the focal zone is closer to the lens than the center of curvature. Wave trajectories in ASCAL, as seen in Figs. 6a-to-6c, suggest that this is always the case since waves are scattered at the input interface towards the acoustic axis, which evidences occurrence of negative refraction. Since effective index increases in absolute value toward the output interface, the rays are bent towards the acoustic axis. A ray incident on a "unit" in the innermost layers might be refracted not only negatively but also positively depending on the moduli of its wave vector, the wave vector of the lens in the direction of one dimensional periodicity and the corresponding wave vector in air [9]. Since the focal zones reside between the inner vertex of the lens and the center of curvature, positive refraction can only take place for rays reaching the output interface above the normal to the surface. This possibility cannot be ruled out at once because positive refraction at the input interface (see Fig. 5b), which leads to divergent waves with respect to the acoustic axis, can also occur via the third band. Besides, birefraction that is likely to occur for ν between approximately 9.5 kHz and 10.5 kHz for $R_{min} = 300$ mm can also contribute to formation of dual foci [11]. For $R_{min} \geq 500$ mm, E is smaller than 0.17, for which the second and third bands in Fig. 5a just begin to overlap in range, thus contribution via birefraction can be disregarded. Therefore, it can be confidently said that negative refraction at both interfaces of ASCAL accompanied by index guiding is the main focusing mechanism, while geometric effects and self collimation are responsible for dual focusing behavior.

Transverse focal size can be reduced further to achieve sub-wavelength resolution by introducing a gradient either in the filling fraction and/or in the densities along the transverse direction. Besides, mapping into elliptical arcs instead of circular ones might also be beneficial in this sense, and help to eliminate the double focusing.

4. CONCLUSION

ASCAL obtained by modifying a triangular SC so that each column lies on concentric circular paths, is shown to focus acoustic waves effectively by means of FEM computations and FDTD simulations. Sharp focusing, for which longitudinal and transverse confinements are of the order of acoustic wavelength in air for a set of R_{min}, is observed at particular frequencies. Focusing properties of the lens are discussed by considering BSs and EFCs of elongated triangular SCs. It is argued that, negative refractions taking place at the ASCAL-air interfaces and bending of waves towards acoustic axis due to gradually-varying effective index of refraction are responsible for focusing of plane waves. Dual focusing behavior is explained via geometric effects and self guiding. Possible contribution of birefraction to dual foci is also discussed.

Although focal distance is found to increase with increasing R_{min} and ν, variation of focal length and spot size with R_{min} revealed no significant correlation obeying a formulation, such as the lensmaker's formula. Therefore, ASCAL presents negative-dispersive behavior where waves with higher frequencies are focused further.

The proposed ASCAL has various potential implementations, such as ultrasonic imaging in medical sciences. Large numerical aperture offered by ASCAL is beneficial for better resolution in acoustic microscopes.

REFERENCES

1. M. S. Kushwaha, P. Halevi, G. Martinez, et al., Phys. Rev. B **49**, 2313 (1994).
2. C. Goffaux and J. P. Vigneron, Phys. Rev. B **64**, 075118 (2001).
3. J. O. Vasseur, P. A. Deymier, A. Khelif, et al., Phys. Rev. E **65**, 056608 (2002).
4. J. V. Sánchez-Pérez, D. Caballero, R. Mártinez-Sala, et al., Phys. Rev. Lett. **80**, 5325 (1998).
5. A. V. Grigor'evskii, V. I. Grigor'evskii, and S. A. Nikitov, Acoust. Phys. **54**, 289 (2008).
6. V. Burov, K. Dmitriev, and S. Sergeev, Acoust. Phys. **55**, 298 (2009).
7. L. Feng, X.-P. Liu, Y.-B. Chen, et al., Phys. Rev. B **72**, 033108 (2005).
8. L. Y. Wu, L. W. Chen, and R. C. C. Wang, Phys. B: Condens. Matter **403**, 3599 (2008).
9. A. Sukhovich, L. Jing, and J. H. Page, Phys. Rev. B **77**, 014301 (2008).
10. L. Feng, X.-P. Liu, M.-H. Lu, et al., Phys. Rev. Lett. **96**, 014301 (2006).
11. M.-H. Lu, C. Zhang, L. Feng, et al., Nature Mater. **6**, 744 (2007).

12. V. Gulyaev and G. Ivanchenko, Acoust. Phys. **50**, 140 (2004).

13. F. Cervera, L. Sanchis, J. V. Sánchez-Pérez, et al., Phys. Rev. Lett. **88**, 023902 (2001).

14. C.-H. Kuo and Z. Ye, J. Phys. D: Appl. Phys. **37**, 2155 (2004).

15. A. Hakansson, F. Cervera, and J. Sanchez-Dehesa, Appl. Phys. Lett. **86**, 054102 (2005).

16. A. Martinez, H. Miguez, A. Griol, et al., Phys. Rev. B **69**, 165119 (2004).

17. S. He, Z. Ruan, L. Chen, et al., Phys. Rev. B **70**, 115113 (2004).

18. T. Matsumoto, K. S. Eom, and T. Baba, Opt. Lett. **31**, 2786 (2006).

19. E. Ozbay, K. Aydin, I. Bulu, et al., J. Phys. D: Appl. Phys. **40**, 2652 (2007).

20. C. Qiu, X. Zhang, and Z. Liu, Phys. Rev. B **71**, 054302 (2005).

21. E. Vinogradov, V. Babintsev, V. Veselago, et al., Phys. Wave Phenom. **15**, 126 (2007).

22. A. Sukhovich, B. Merheb, K. Muralidharan, et al., Phys. Rev. Lett. **102**, 154301 (2009).

23. E. Foca, H. Foll, F. Daschner, et al., Phys. Status Solidi A **202**, R35 (2005).

24. S.-Y. Yang, C.-Y. Hong, and H.-C. Yang, J. Opt. Soc. Am. A **23**, 956 (2006).

25. H. Kurt, E. Colak, O. Cakmak, et al., Appl. Phys. Lett. **93**, 171108 (2008).

26. E. Akmansoy, E. Centeno, K. Vynck, et al., Appl. Phys. Lett. **92**, 133501 (2008).

27. S.-C. S. Lin, T. J. Huang, J.-H. Sun, et al., Phys. Rev. B **79**, 094302 (2009).

28. K. Deng, Y. Q. Ding, Z. J. He, et al., J. Phys. D: Appl. Phys. **42**, 185505 (2009).

29. T. Daniel and S.-D. José, New J. Phys. **9**, 323 (2007).

30. V. Espinosa, V. J. Sánchez-Morcillo, K. Staliunas, et al., Phys. Rev. B **76**, 140302 (2007).

31. J. Shi, S.-C. S. Lin, and T. J. Huang, Appl. Phys. Lett. **92**, 111901 (2008).

32. Z. He, F. Cai, Y. Ding, et al., Appl. Phys. Lett. **93**, 233503 (2008).